Influence of boundary conditions and confinement on nonlocal effects in flows of wormlike micellar systems

Chloé Masselon and Annie Colin*
LOF, Unité Mixte CNRS, Rhodia, Bordeaux 1, 178 Avenue du Docteur Schweitzer, F-33608 Pessac Cedex, France

Peter D. Olmsted
School of Physics and Astronomy, University of Leeds, Leeds LS2 9JT, United Kingdom
(Received 31 July 2009; revised manuscript received 22 December 2009; published 9 February 2010)

In this paper we report on the influence of different geometric and boundary constraints on nonlocal (spatially inhomogeneous) effects in wormlike micellar systems. In a previous paper, nonlocal effects were observable by measuring the local rheological flow curves of micelles flowing in a microchannel under different pressure drops, which appeared to differ from the flow curve measured using conventional rheometry. Here we show that both the confinement and the boundary conditions can influence those nonlocal effects. The role of the nature of the surface is analyzed in detail using a simple scalar model that incorporates inhomogeneities, which captures the flow behavior in both wide and confined geometries. This leads to an estimate for the nonlocal "diffusion" coefficient (i.e., the shear curvature viscosity) which corresponds to a characteristic length from 1 to 10 μm.

DOI: 10.1103/PhysRevE.81.021502 PACS number(s): 83.80.Qr, 83.60.Fg, 83.85.Ei

I. INTRODUCTION

Complex fluids such as polymers, liquid crystals and surfactant solutions have a mesoscopic structure that is readily perturbed by flow [1]. For example, wormlike micelles, which are long and cylindrical aggregates of self-assembled surfactants, can be strongly modified by a shear flow. Indeed, shear can stretch or break the micelles, entangle and disentangle the micellar network, or even increase their length [2]. Those systems thus display highly non-Newtonian behavior, and often exhibit a characteristic flow curve [measured shear stress as a function of shear rate $\sigma(\dot{\gamma})$] with a stress plateau σ^* separating two branches of high and low viscosity, corresponding to different structures [3]. This is characteristic of shear banding. During the last decade, studies on such systems have led to a consistent picture of the flow behavior on the stress plateau: for applied shear rates in the plateau region, macroscopic bands of different $\dot{\gamma}$ and different micellar orientations can coexist along the stress plateau. A viscously thicker (nascent) fluid and a thinner (shear-induced) fluid flow side-by-side, and the proportion of the shear-induced structure grows as a function of $\dot{\gamma}$ on the stress plateau. In a classical Couette or cone-and-plate geometry (with gap sizes of order a millimeter) and for a given system, the position of the interface between the two structures lies at a fixed value of the shear stress, corresponding to the stress plateau σ^*; this has been shown both experimentally [4–6] and theoretically [7–9].

We recently showed that this stress selection appears to break down in *confined* geometries with much smaller gap sizes [10]. Upon measuring the velocity profiles of micelles flowing under a drop of pressure in a straight microchannel of width ~ 100 μm, we found that the shear stress value at the interface between the two shear bands increases as a function of the applied pressure drop; correspondingly, the relation linking the local shear rate to the local shear stress broke down such that the apparent measured flow curve disagreed with that obtained form conventional rheometry geometries. This suggests that nonlocal and finite size effects are important at such small channel widths. This is in line with recent theoretical developments about shear-banded flows [7]. In the past decades, much theoretical work has been devoted shear banding. In order to account for the existence of two structures, Spenley *et al.* [11] used a reptation-reaction model that generalized Doi-Edwards theory for entangled polymers, and proposed a constitutive law. They calculated a multivalued flow curve exhibiting two stable branches separated by an unstable zone where σ decreases as a function of $\dot{\gamma}$. Those early models did not select a precise value of the shear stress σ^* at which shear banding occurs. Subsequently, various criteria such as the minimization of an effective free energy under flow [12], boundary conditions on the normal stress in a pipe geometry [13], or local maximum on the flow curve, were proposed to capture stress selection.

A major improvement was achieved by taking into account diffusion terms in the constitutive equations [7,9,14–18]. The introduction of spatial derivatives of the shear stress can be justified rigorously using the Fokker-Planck equation for simplified microscopic models such as the dumbbell model [19]. In this case, the stress flux arises from Brownian motion of the polymer chains to-and-fro across the interface. Although this movement does not produce a net matter flux, it produces a nonzero net stress flux as the chains on the low shear-rate side of the interface carry more shear stress than the chains on the high shear-rate side of the interface. Another mechanism for such a stress transfer across the interface could be the propagation of the interactions between the chains, such as short range van der Waals or hard core interactions, long range Coulombic or hydrodynamic interactions, and polymer stiffness [7,20].

*annie.colin-exterieur@eu.rhodia.com

In all these models, the resulting equation governing the flow is a spatial differential equation (mathematically, a nonlinear reaction-diffusion equation) for the microstructure (such as a nematic order parameter, the polymer deformation or polymeric contribution to the stress), which requires boundary conditions. The introduction of diffusion terms in the constitutive equation allows the selection of a unique value for the shear stress plateau in a wide geometry [16,18,21]. However, it also induces a breakdown of the local flow curve, since flow at any position in the sample is influenced by its neighborhood. If the interfacial width is much smaller than the distance between walls, then the local flow curve should be followed except for in the vicinity of the interface [21,22]. For small gaps one expects the stress to deviate slightly from the wide gap limit [9]. Finally, we note that the physically relevant or correct choice of boundary condition has not yet been settled upon, despite some study of this [20,23,24].

In our previous work, we used a simple scalar model (see below for details) to account for the velocity profiles of micelles flowing in a straight microchannel. This model contained a nonlocal ("diffusive") term whose coefficient defined a characteristic length scale ξ. We were able to fit the velocity profiles and account for the increase in the shear stress plateau value as a function of the drop of pressure across the microchannel. The length scale for ξ deduced from these experiments, of order a few μm, agrees with recent indirect measurements [25] on the same wormlike micellar solution. This is much larger than the mesh size ξ_{mesh} which may be estimated from the elastic modulus by $\xi_{mesh}=(\frac{k_bT}{G})^{1/3}$. For our system, we get $G=70$ Pa and $\xi_{mesh}=39$ nm. The origin of this large length scale is still unknown: candidate mechanisms include concentration, or local changes in micelle length or branching.

In this work, we perform experiments in a confined geometry, and address the question of both the nature of boundary conditions and the degree of confinement [20]. This article is organized as follows. Section II is devoted to the description of the experimental procedure. First, classical rheology experiments performed in a wide Couette cell are described, followed by experiments performed in confined geometries. We report on the preparation of channels with various surfaces: rough glass, smooth glass, and polydimethylsiloxane (PDMS). We describe the particle image velocimetry (PIV) device that allowed us to measure velocity profiles in microchannels, and we recall how local rheological measurements are extracted from these data. Section III describes the wormlike micellar system under study, including the linear response of the system and the flow curve measured in a wide cone-and-plate cell geometry. Section IV deals with the measurements in the different kinds of microchannels, in which the degree of confinement and the nature of the surfaces are varied. In Sec. V we summarize some of the main predictions of nonlocal models with various boundary conditions, and then we analyze our data within this framework in Sec. VI. The final section is devoted to discussion and conclusion, and an Appendix contains details of the calculations.

II. EXPERIMENTAL PROCEDURE AND SETUP

A. Global rheological experiments in cone-and-plate cell

To study the effect of shear flow on the complex fluid under study, we used a TA Instruments ARG2 rheometer and a sanded cone-and-plate cell. The radius of the cone is $R=2$ cm and the cone angle is $\alpha=2°$, so that the maximum gap was $2e_{max}\simeq 1400$ μm. The rheometer imposes a torque Γ on the axis of the Couette cell which thus induces a shear stress σ in the fluid. The rotation speed ω of the cone-and-plate cell is continuously recorded, from which the shear rate $\dot{\gamma}$ can be deduced. A computer-controlled feedback loop on the applied torque Γ can also be used to apply a constant shear rate without any significant temporal fluctuations ($\delta\dot{\gamma}/\dot{\gamma}\simeq 1\%$). In a cone-and-plate geometry, and in the limit of low inertia, i.e., for low rotation speeds, the shear stress is homogeneous and constant in the whole geometry. The shear stress σ and the shear rate $\dot{\gamma}$ indicated by the rheometer are related to Γ and ω by the following relations:

$$\sigma=\frac{3\Gamma}{2\pi R^3}, \tag{1}$$

$$\dot{\gamma}=\frac{\omega}{\tan\alpha}. \tag{2}$$

At this stage, it is important to note that the shear rate $\dot{\gamma}$ given by the rheometer may differ from the true shear rate in the sample when wall slip, inhomogeneous or unstable flows are present. A sanded geometry reduces the effects of wall slip. We measured the linear response of the sample as a function of frequency, and the flow curve (obtained from the measured torque as a function of applied rotation rate). For this purpose, we apply increasing rotation (average shear) rates for 2000 s/step, in intervals $\delta\dot{\gamma}=0.5$ s^{-1} for $\dot{\gamma}<1$ s^{-1} and $\delta\dot{\gamma}=1$ s^{-1} for $\dot{\gamma}>1$ s^{-1}. These conditions ensured steady state. To compute the equilibrium value, we average the stress measurement over the last 600 s. These experiments allow us to probe the rheological properties of the fluid in a wide geometry. In the following, we describe the experimental procedure that we used to study the flow of the micellar system in a confined geometry.

B. Preparation of the microdevices

The aim of this work is to study the influence of both confinement and boundary conditions on the flow of wormlike micelles. For this purpose, straight microchannels made of three different materials were prepared. Those microchannels are straight with rectangular cross sections or "canyons" (Fig. 1), with aspect ratios (height divided by width) from $\simeq 5-10$, so that the flow in these channels can be safely assumed to be that of flow between two infinite parallel planes [26]. The length of the microchannel varies between 7 and 14 cm.

In order to influence the boundary conditions of the flow, either the nature of the surface or its roughness are varied.

(i) S1 (glass)—Smooth glass surfaces were obtained using commercial rectangular capillary tubes (composite metal service) of inner dimensions 0.2×4 mm^2. Typical electronic

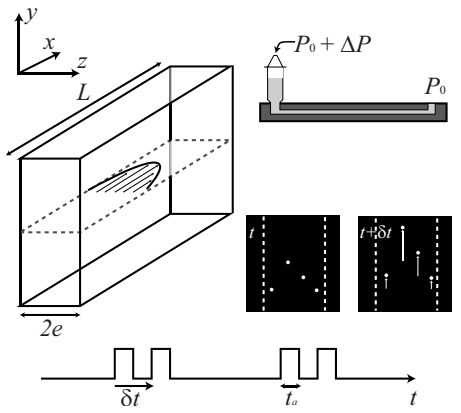

FIG. 1. Schematic view of the canyon geometry, L is the length of the microchannel and $2e$ its width. Bottom: schematic temporal acquisition of the images using the PIV device, where t_a is the acquisition time of each image and δt the time interval between two frames. Above are shown two schematic frames with tracers in the x-z plane and the corresponding velocity vectors dx estimated using standard cross-correlation algorithms.

microscopy pictures of the internal glass surfaces of such capillaries [Fig. 2(d)] demonstrate that the surfaces are smooth and optically flat. The wormlike micellar solutions wet the glass. The capillary is connected to the syringe as follows: tubing runs from the sample syringe needle tip to another needle tip. A hole is then made in the other end of this second tip (which would usually insert into a syringe), and the capillary tube is inserted into this hole. To enhance the seal the tube and the syringe needle are glued together on a glass slide, which forms a perfect connection.

(ii) R1, R2 (rough)—Rough boundary conditions were obtained by following the experimental procedure described in Ref. [27]. Two glass slides (1 mm thick) are glued to a first

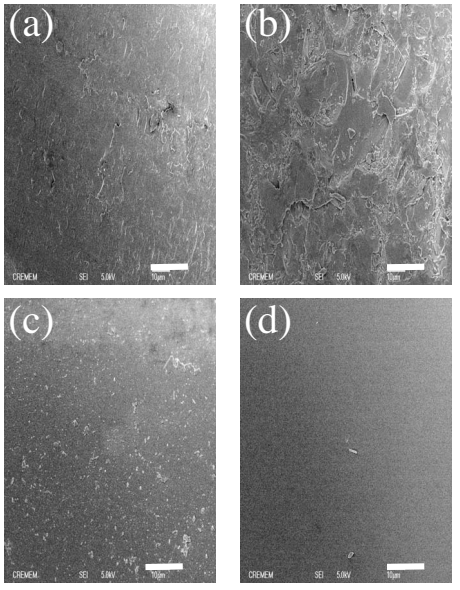

FIG. 2. Electronic microscopy pictures of the surfaces. (a) Rough glass surface R1; (b) rough glass surface R2; (c) smooth coated film of PDMS on glass (S2); and (d) smooth glass S1 from a capillary tube (composite metal service). The size of bar is 20 μm.

glass slide with an optical adhesive (NOA 81, Norland Products) to form a channel of controlled width with a spacer of size $2e$. The roughness of the side walls of the channel is due to the roughness of the edges of the 1 mm thick glass slides [see Fig. 2(c)]. Access holes are made in a second glass slide with sand blasting. The channel is then sealed to this glass slide using the same optical adhesive. An optical adhesive is then used to block the holes that appear on the edge. The distance between the two glass walls is measured under a microscope to get the real dimension of the channel. Nanoport connections are glued on the access holes and allow to connect the sample syringe to the channel.

(iii) S2 (PDMS)—We first tried to prepare PDMS microfluidic devices using standard lithography procedures [28]. However, PDMS is very weak and deforms easily under the flow of viscous fluids. Hence we used the same procedure as for R1 and R2, with PDMS coated on the edges of the 1 mm thick glass slides. The PDMS layer is 20 μm thick. The wormlike micellar solution does not wet the PDMS surface. This allowed us to prepared microchannels with PDMS on the lateral walls, but that can also sustain high pressure drops because it is made of glass.

All the above devices are confined "canyon" geometries, with dimensions 100–220 μm$\times$1 mm.

C. Local rheological measurements in a confined geometry

The geometry of the flow in the microfluidic devices is shown in Fig. 1. Since all geometries have aspect ratios (height divided by width) larger than 5, the flow at the middle height of these channels can be approximated as between two infinite plates. A syringe filled with a given sample is directly connected to the inlet of the straight channel and connected to a pressure controller (Fluigent) that can impose controlled pressure drops in the $\Delta P = 50$–2000 mbar range. The velocity profiles in the microchannels are then classically measured using PIV [29]. The fluid is seeded with small fluorescent tracers (Invitrogen Fluorospheres, 1 μm diameter and concentration of 0.001 wt %). In the canyon geometry images of the flowing tracers are acquired using an inverted fluorescent microscope at the middle height of the channel using a 40$\times$ magnification objective. With this objective the entire width $2e$ of the channel in the x-z plane can be captured in one single view, and with a small depth of field of $\approx$1 μm. This was not possible for the commercial capillary tube (i.e., the S1 surfaces), since the round shape in the x-y plane disrupts optical imaging. We thus have to image the flow by looking through the flat side in the x-y plane. To that aim, a high numerical aperture objective was used (60$\times$, N.A. 1.2, oil immersion), to access slices of the flow with a small depth of field of about 0.5 μm, mounted on a piezoactuator (Polytech PI, PIFOC) to scan the z direction of the flow. In this geometry, each plane of imaging therefore corresponds to a unique velocity.

A charge-coupled device (CCD) camera coupled to an intensifier (Hamamatsu and R&D vision) allows us to record pairs of images with well-defined acquisition times $t_a \simeq 100$ ns$=1$ ms (see Fig. 1). Pairs of images are taken at a

fixed time interval $\delta t \simeq 3\ \mu s - 1$ s. A classical algorithm of cross-correlation (developed using MATLAB) between two images of a pair determines the translation dx along the flow, and thus the velocity $dx/\delta t$. In the canyon geometry and the commercial glass capillary several pairs of images are needed to accurately estimate the velocity profile using statistical averaging ($\approx$200 for the canyon and $\approx$200 pairs per slice for the commercial capillary). In our experiments dx is a scalar since the flow is unidirectional, but it depends on z. Local velocities can be resolved up to 1 m/s with a spatial resolution $dz \simeq 1\ \mu$m in the plane of the flow.

For all the microdevices, the images are acquired far enough from the inlet of the channel to measure fully developed profiles and eliminate entrance effects [30]. From these profiles, the local rheological flow curves are extracted following Ref. [31]. In our geometry with a high aspect ratio the stress distribution is well-approximated by

$$\sigma(z) = \frac{\partial P}{\partial X} z \tag{3}$$

at a given position z from the centerline of the microchannel. In the limit of wide aspect ratios and an infinite length channel a simple force balance leads to the following expression for the wall shear stress,

$$\sigma_w = \frac{\Delta P e}{L}, \tag{4}$$

where ΔP is pressure difference between the two ends of the channel of length L and thickness $2e$. Rough estimates of the entrance and exit lengths for shear thinning fluids [30] are less than 70 μm, which is at least a hundred times smaller than the length of the channel (at least 50 mm). Moreover, because the local shear rate $\dot{\gamma}$ is simply given by the local slope of the velocity profile $v(z)$, each position z in the channel corresponds to a pair $(\sigma, \dot{\gamma})$. Hence from a single profile $v(z)$, we can access the whole constitutive curve, shear stress σ as a function of shear rate $\dot{\gamma}$.

III. EXPERIMENTAL SYSTEM: 6% CPCL-SAL IN BRINE

The system under scrutiny is a solution of cetylpyridium chloride and sodium salicilate at a molar ratio [Sal]/[CPCl]=0.5, in salted water at 0.5 M of NaCl (abbreviated CPCl-Sal in the following). We focus on a concentration ϕ=6% and a temperature of 22 °C, which is in the semidilute regime and at a concentration far from the isotropic-nematic transition, has been widely studied. To perform PIV experiments we seed the solution with small fluorescent latex particules (Invitrogen Fluorospheres 1 μm diameter, concentration 0.001 wt. %). Rheological measurements (Fig. 3) demonstrate that the sample is a true Maxwell fluid, with the relaxation time $\tau_r \simeq 4$ s and elastic modulus $G_0 \simeq 70$ Pa extracted from the fit to the Maxwell model. The beads probably modify the rheological properties of this system, since Berret *et al.* [32] found the values τ_r =990 ms and G_0=62 Pa in the absence of tracers.

The steady state non linear flow curve measured as described above is shown in Fig. 4. The flow curve has two

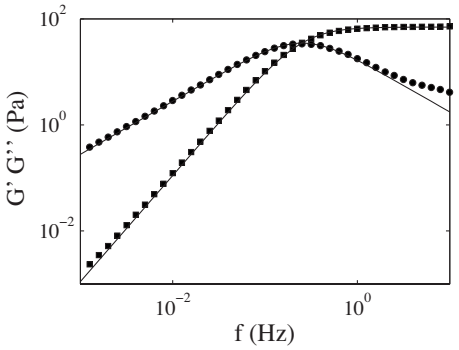

FIG. 3. Real (G') and imaginary (G'') linear rheological response as a function of the frequency f, for a 6% CPCl-Sal mixture in brine solution. The sample is seeded with 0.001 wt % latex beads. The lines correspond to the Maxwell model. The relaxation time τ_r=4 s and the elastic modulus G_0=70 Pa are extracted from the fit of the data to this model.

branches: at low shear rate, the fluid is Newtonian with a viscosity η_1=20.6 Pa s, while at high shear rates Bingham behavior is observed, of the form $\sigma = A + \eta_2 \dot{\gamma}$ [6]. These two branches are separated by a stress plateau at σ^*=54 Pa, which extends from $\dot{\gamma}_1$=8 s^{-1} to $\dot{\gamma}_2$=24 s^{-1}. As for the linear rheological data, these values differ slightly from those reported by Berret *et al.* [32] ($\sigma^\star$=52 Pa) or Salmon *et al.* [6] ($\sigma^\star$=65 Pa, $\dot{\gamma}_1$=2.5 s^{-1}, $\dot{\gamma}_2$=26 s^{-1}). We believe that the introduction of latex spheres, some impurities, and/or the slight difference in temperature are responsible for these discrepancies.

We now study the flow behavior in the confined geometries described above. Following the classical picture, in the low shear stress region (i.e., in the center of the microchannel) one should observe only the nascent viscous fluid only. Above a critical pressure gradient the low viscosity shear-induced structure is expected to appear near the two lateral walls. One also expects that the interface between the two

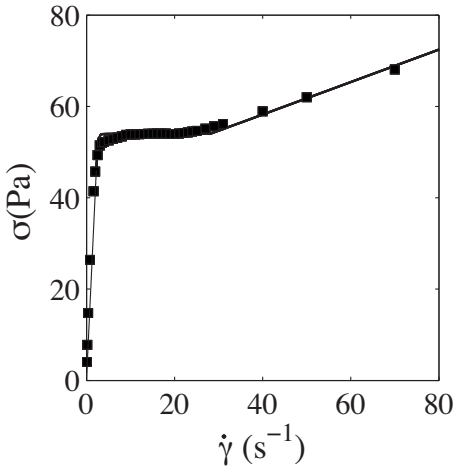

FIG. 4. Global flow curve from a rheometer using a cone-and-plate cell, with shear stress σ and the shear rate $\dot{\gamma}$ defined by Eqs. (1) and (2). The stress plateau occurs at $\sigma^\star$=54 Pa. The sample is seeded with 0.001 wt % latex beads. The line corresponds to the flow curve predicted in wide plate geometry by the nonlocal model (see Sec. IV).

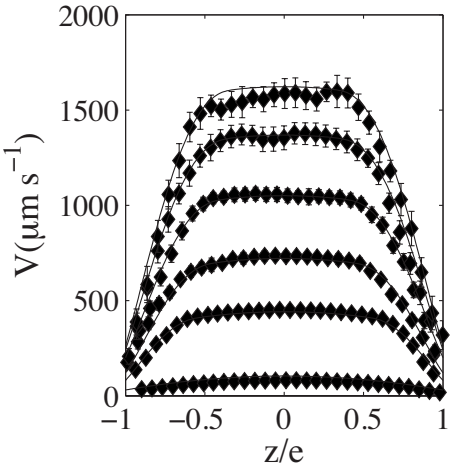

FIG. 5. Velocity profiles at different ΔP (wall stresses σ_w =46,65,74,78,83,87 Pa from bottom to top) for channel width $2e$=120 μm and rough surface R2. Solid lines are calculated using the nonlocal model described Sec. V with the same fitting parameters η_1=20.6 Pa s, η_2=0.35 Pa s, A=44 Pa, γ_1=5.6 s^{-1}, κ =10^{-10} Pa s m^2.

structures lies at a position z_{int} where the local stress is equal to the shear stress plateau σ^*,

$$z_{\text{int}} = \frac{\sigma^* L}{\Delta P}. \tag{5}$$

IV. FLOW IN MICROCHANNELS

A. Influence of the confinement—rough surface R2

Figure 5 shows velocity profiles at different ΔP as a function of the normalized coordinate z/e for the rough surface R2, with channel width $2e$=120 μm. Significant slippage is observed at every value of the wall shear stress σ_w. The slip velocities V_s are determined by linear fits of the last points of the velocity profiles near the walls (Fig. 6). The slip velocities increase with the applied shear stress at the wall (V_s =$A\sigma_w^\alpha$ with α=3.5), yet their contributions to the maximal

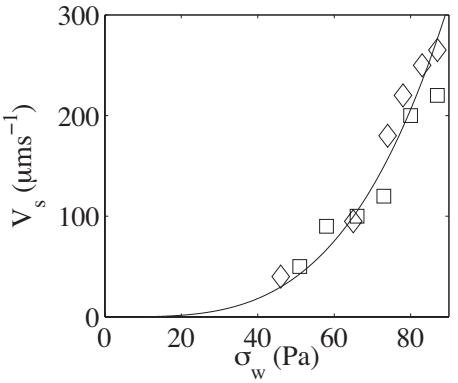

FIG. 6. Slip velocity V_s as a function of the wall shear stress σ_w for R2 surfaces for two microchannels with different widths (□ to R2 $2e$=200 μm, ◇ to R2 $2e$=120 μm). The line corresponds to the equation V_s=0.000045$\sigma_w^{3.5}$.

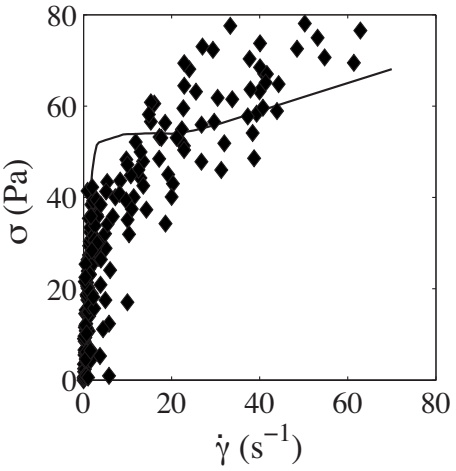

FIG. 7. Solid line: global flow curve from a rheometer using a cone-and-plate cell, with shear stress σ and the shear rate $\dot{\gamma}$ defined by Eqs. (1) and (2). Points (◇): local flow curve deduced from the velocity profiles for different wall shear stress (σ_w =46,65,74,78,83,87 Pa). The local shear rate is the derivative of the velocity profile and the local shear stress is calculated using Eq. (3). The velocity profiles are measured in a $2e$=120 μm thick microchannel made with rough R2 surfaces.

velocity V_m remain almost constant (V_s<0.15 V_m). Let us now consider the flow inside the cell. For the smallest applied σ_w, the velocity profiles correspond to Poiseuille-like flow. For applied shear stress at the wall σ_w=53.8 Pa, thin highly sheared bands nucleate at the two lateral walls. This value of shear stress is slightly smaller than the plateau shear stress measured in cone and plate geometry. We will comment this point below. For higher σ_w, the width of these bands increases, and the profiles display a plug flow shape, with low viscosity bands near the walls.

We deduce the local rheological behavior from the velocity profiles using the procedure outline above [31], leading to the local flow curves depicted in Fig. 7. There is some agreement with the flow curve measured in the shear-rate controlled mode of a rheometer, using a sanded cone-and-plate geometry that is similar to the rough surface R2. However, the two measurements only agree for $\dot{\gamma}$<4 s^{-1}, corresponding to the highly viscous branch of the nascent fluid. For higher shear rates significant discrepancies are observed, and the rheological behavior of the highly sheared branch in the microchannel varies as a function of the applied pressure drop.

We now focus on the values of the stress σ_{int} at the interface between the two bands. The position of the interface z_{int} can easily be determined from the sharp change in the slope of the velocity profiles. The corresponding stress σ_{int} is computed using Eq. (5) and reported on Fig. 8 as a function of σ_w (see the darkest points). Clearly, σ_{int} varies considerably with the applied shear stress at the wall, and is less than σ^* measured in the wider cone and plate geometry. In other words, the shear-induced band occupies a larger fraction (smaller z_{int}) with increasing shear stress at the wall, than it would if the stress at the interface remained constant. Note that local velocimetry experiments were performed on the same system in a Couette cell (with a shear stress gradient ten times less

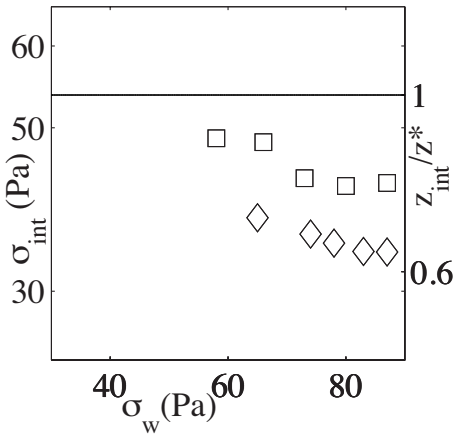

FIG. 8. Shear stress at the interface between the two bands and z_{int}/z^* as a function of the shear stress at the wall for various geometries and surfaces. The line corresponds to the plateau value $\sigma^*=54$ Pa measured in cone-and-plate geometry (□ to R2 $2e=200$ μm, ◇ to R2 $2e=120$ μm).

than here) [6] and in large pipes (of 20 cm diameter, much less confined than here) [33–35], and were consistent with an invariant $\sigma_{\text{int}}=\sigma^*$.

Hence, the experiments here show that a simple description using a homogeneous constitutive curve $\sigma=f(\dot{\gamma})$ and a unique value of σ^* is not sufficient to describe the flow over the whole range of pressure drops studied. We will show below that a consistent description arises by considering a fully nonlocal description of the rheology.

The same experiments were performed in a wider channel $2e=200$ μm for surface R2, with qualitatively similar results to those found in the smaller channel (Fig. 9). Shear banded flows are observed for high shear stress at the wall. As previously, significant slippage is observed at every value of the wall shear stress σ_w. As displayed on Fig. 6, the slip velocity does not depend upon the size of the microchannel. The data extracted from the velocity profile in a $2e$

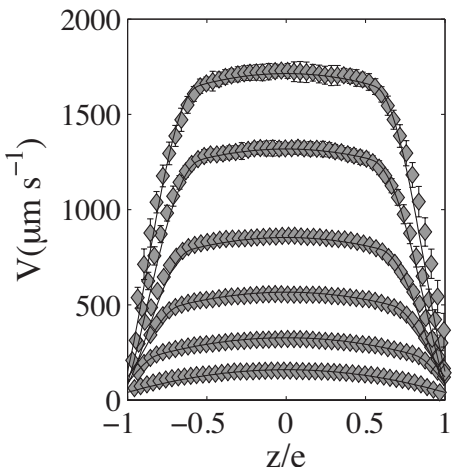

FIG. 9. Velocity profiles for different ΔP (wall stresses $\sigma_w=51,58,66,73,80,87$ Pa from bottom to top), for channel width $2e=200$ μm with rough surface R2. Solid lines are calculated using the nonlocal model described in Sec. V with $\eta_1=20.6$ Pa s, $\eta_2=0.35$ Pa s, $A=44$ Pa, $\gamma_1=5.6$ s^{-1}, $\kappa=10^{-10}$ Pa s m^2.

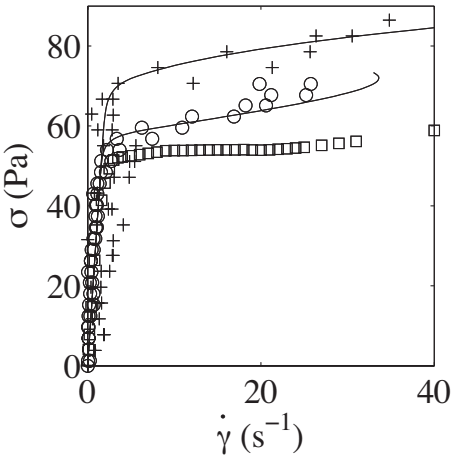

FIG. 10. Global flow curve from a rheometer using a cone-and-plate cell (□), with shear stress σ and the shear rate $\dot{\gamma}$ defined by Eqs. (1) and (2). (○): local flow curve deduced from the velocity profiles for a shear stress at the wall equal to $\sigma_w=80$ Pa. (+): local flow curve deduced from the velocity profiles for a shear stress at the wall equal to $\sigma_w=94$ Pa. The local shear rate is the derivative of the velocity profile and the local shear stress is calculated using Eq. (3). Solid lines are calculated using the nonlocal model described in Sec. V with $\eta_1=20.6$ Pa s, $\eta_2=0.35$ Pa s, $A=44$ Pa, $\gamma_1=5.6$ s^{-1}, $\kappa=10^{-10}$ Pa s m^2. The velocity profiles are measured in a $2e=200$ μm thick microchannel made with rough R2 surfaces.

$=200$ μm and in a $2e=120$ μm collapse on a single curve. However, the local flow curves extracted from the velocity profiles measured in the microchannel agree much better with measurements in the cone-and-plate geometry (Fig. 10); noticeable discrepancies occur only for a few points at high shear stress. Figure 8 shows that the stress at the interface σ_{int} between the bands extracted from these velocity profiles decreases slightly as a function of the applied shear stress at the wall (see □ in Fig. 8). The stresses in the wide channel are closer than those in the narrow channel to the plateau value measured in the cone-and-plate geometry.

This suggests that the discrepancy between local and global rheology vanishes in thicker microchannels, so that increasing the thickness of the microchannel allows us to recover the measurements performed in the wide gap classical geometry. The value of the shear stress at the interface between the two bands varies not only as a function of the pressure drop, but also as a function of the confinement. This clear finite size effects cannot be understood using the classical (homogeneous) flow curve.

B. Influence of the surface

We next consider the effect of the surface itself: we keep the channel thickness fixed at $2e=200$ μm and study another rough glass surfaces (R1), a smooth glass surface (S1) and a PDMS smooth surface (S2). To accurately compare the flow in the various microchannels (see Fig. 11), we correct the velocity profiles by removing the slip velocity. The data for the slip velocity as a function of the shear stress at the wall are reported in Fig. 14. In all cases, at low applied σ_w the velocity profile is that of Poiseuille flow of a Newtonian

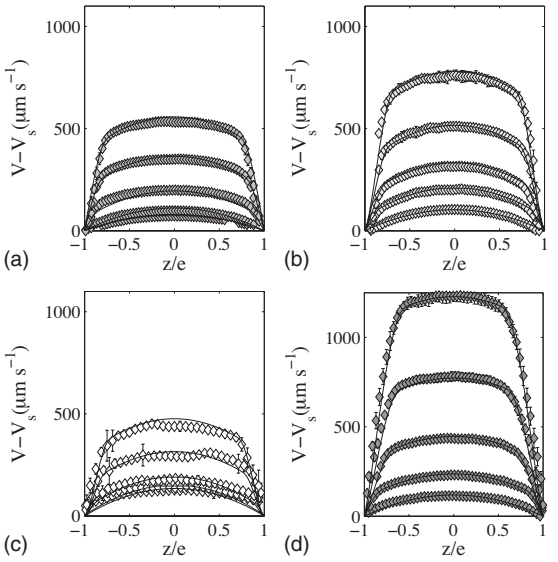

FIG. 11. Velocity profiles corrected by the slip velocities for different ΔP for various geometries. Solid lines are calculated using the nonlocal model described Sec. V with the same fitting parameters $\eta_1=20.6$ Pa s, $\eta_2=0.35$ Pa s, $A=44$ Pa, $\gamma_1=5.6$ s^{-1}, $\kappa=10^{-10}$ Pa s m^2. Top left: $2e=200$ μm thick microchannel with rough surfaces R1. Wall shear stresses (bottom to top) $\sigma_w=33,42,50,58,66$ Pa. Top right: $2e=200$ μm thick microchannel with smooth PDMS surfaces (S2). Wall shear stresses (bottom to top) $\sigma_w=38,54,62,70,77.5$ Pa, Bottom left: $2e=200$ μm thick microchannel with smooth glass surfaces (S1). Wall shear stresses (bottom to top) $\sigma_w=55,60,65,70,75$ Pa. Bottom right: $2e=200$ μm thick microchannel with rough surfaces (R2). Wall shear stresses (bottom to top) $\sigma_w=51,58,66,73,80$ Pa.

fluid. At higher applied stresses (pressure drops) the shear-induced band appears near the walls. Let us now analyze in details the shape of the velocity profiles and the flow near the wall (i.e., slip velocity and shear rate at the wall) as a function of the nature of the surface.

Quantitatively, striking differences are observed between the various surfaces. Let us first report on the position of the interface between the bands as a function of the shear stress at the wall. Figure 12 shows that the value of the shear stress at the interface between the two bands differs from σ^* measured in the wider cone and plate geometry. The position occupied by the shear-induced phase may be greater (R2, S2) or smaller (S1 and in some cases R1) than it would if the stress at the interface remained constant. The maximal value V_{max} of the slip-corrected velocity also depends on the nature of the surface. For wall shear stress $\sigma_w=70$ Pa we find $V_{max}=516$ μm s^{-1} for S2 (smooth PDMS) and $V_{max}<314$ m s^{-1} S1 (smooth glass). This large difference is caused by the different values of the shear rate at the wall. We measure shear rate at the wall by taking the slope of linear fits of the last points of the velocity profiles near the walls. Figure 13 shows the relation between wall shear rate and wall shear stress. Strikingly, these laws differ from the bulk rheology. Almost none of these points fall on the globally measured flow curve. It seems that for high shear stress, the wormlike micelles are more viscous near the surface than in the bulk. Note that these data do not depend

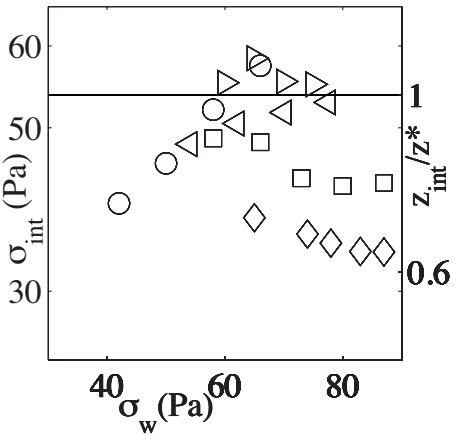

FIG. 12. Shear stress at the interface between the two bands and z_{int}/z^* as a function of the shear stress at the wall for various geometries and surfaces. The line corresponds to the plateau value $\sigma^*=54$ Pa measured in cone-and-plate geometry. (○ correspond to R1, □ to R2 $2e=200$ μm, ◇ to R2 $2e=120$ μm, ◁ to S2, ▷ to S1).

upon the degree of confinement: for the R2 surface the data extracted from the velocity profiles measured in both $2e=120$ μm and $2e=200$ μm microchannels collapse on a single curve.

The surface rheological law thus depends on the nature of the surface, and not on the degree of confinement. Figure 13 also shows that roughness plays a huge role in the flow behavior near the wall. For the same wall shear stress σ_w, the wall shear rates on the smooth glass S1 are very different from those obtained on the rough glass surfaces R1 and R2. The chemical nature of the surface plays a role as well. Wall shear rates are higher (up to a factor of 3) near PDMS surfaces than near glass surfaces for the same wall shear stress. These data allow us to conclude that the relationship between the wall shear rate and the wall shear stress does not primarily depend on the confinement of the flow.

We now analyze the slip velocities. Figure 14 shows the slip velocity V_s as a function of the wall shear stress σ_w. As

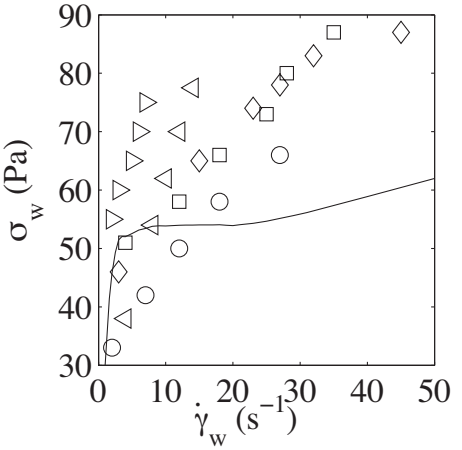

FIG. 13. Wall shear stress as a function of wall shear rate for various geometries and surfaces (○ correspond to R1, □ to R2 $2e=200$ μm, ◇ to R2 $2e=120$ μm, ◁ to S2, ▷ to S1). The line corresponds to the bulk rheology.

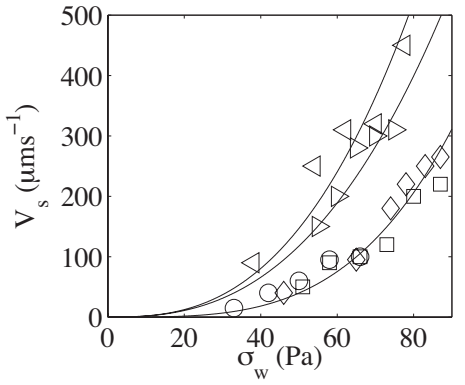

FIG. 14. Slip velocity V_s as a function of the wall shear stress σ_w for various geometries and surfaces (○ correspond to R1, □ to R2 $2e=200$ μm, ◇ to R2 $2e=120$ μm, ◁ to S2, ▷ to S1). From top to bottom the lines correspond to the equation $V_s=0.0038\sigma_w^{2.7}$, $V_s=0.0045\sigma_w^{2.6}$, $V_s=0.000045\sigma_w^{3.5}$.

noticed previously, the slip velocities do not seem to depend upon the thickness of the microchannel: data from the $2e=120$ μm and in a $2e=200$ μm thick microchannels are quite similar for R2 surfaces. The slip velocity increases with the wall shear stress, roughly following a power law $V_s=A\sigma_w^{\alpha}$, with $\alpha=3.5$ for R1 and R2 surfaces, $\alpha=2.7$ for PDMS (S2), and $\alpha=2.6$ for smooth glass (S1). Notably, the slip is weaker on rough surfaces, and the slip is lower on smooth glass than on smooth PDMS. The surface rheological laws are inconsistent with a simple constant drag coefficient, which would arise from the following force balance:

$$\text{Fig. 12} \quad \sigma_w = bV_s. \tag{6}$$

The data are consistent with a "surface drag coefficient" $b(V_s)$ that decreases with increasing V_s; mechanisms could be better alignment of micelles near the surface, or enhanced depletion of micelles near the surface at higher slip velocities.

To conclude this section, our experiments reveal the limitations of the classical global flow curve and finite size effects. The nature of the surface governs the flow in a confined geometry, and the surface rheological law depends upon the chemical nature surface. In the following, we show how it is possible to capture the flow behavior using a nonlocal model.

V. NONLOCAL MODEL

Nonlocal models were introduced to describe smooth structural inhomogeneities during shear banding. These models incorporate spatial gradients of the microstructure of shear rate into the dynamical equations of motion, and give rise to smooth variations of properties between shear bands, with a characteristic interfacial width. The addition of spatial gradients provides a mechanism for stress selection, as discussed already. One of the most studied equation is the diffusive Johnson-Segalman (dJS) model [9,36,37] for the polymeric contribution to the total stress tensor. However, the dJS model predicts a Newtonian shear-induced state $\sigma \sim \dot{\gamma}$, which is not the case in our experiments. Hence, and also for simplicity, we will use a much simpler phenomenological model that captures the Bingham-like nature of the high shear rate branch [6], and is also easy to study analytically. This differs from that measured by Nghe [42] in a cetyl trimethyl ammonium bromide (CTAB) solution, in which the shear-induced structure was a highly shear thinning fluid, $\sigma \sim \dot{\gamma}^{\alpha}$, $\alpha \simeq 0.26$ [43]. Our approach is based on previous models for a scalar order parameter with spatial gradients [38]; we will use a model in which shear-rate gradients contribute to the total stress as in [7,8,18],

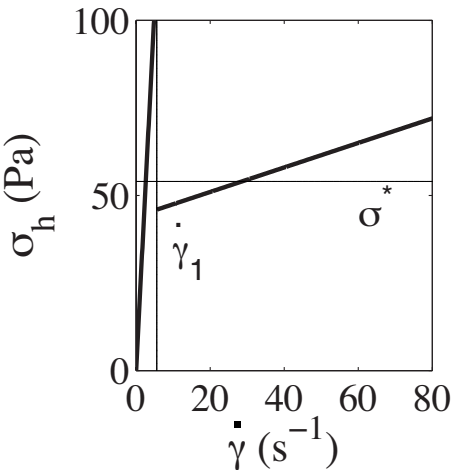

FIG. 15. Homogeneous constitutive relation $\sigma_h(\dot{\gamma})$ to represent the wormlike micelles. The parameters are given by $\eta_1=20.6$ Pa s, $\eta_2=0.35$ Pa s, $A=44$ Pa, $\gamma_1=5.6$ s^{-1}

$$\sigma(z) = \sigma_h[\dot{\gamma}(z)] - \kappa \frac{\partial^2 \dot{\gamma}(z)}{\partial^2 z}, \tag{7}$$

$$\sigma_h(\dot{\gamma}) = \begin{cases} \eta_1 \dot{\gamma} & (\dot{\gamma} < \dot{\gamma}_1) \\ A + \eta_2 \dot{\gamma} & (\dot{\gamma} \geq \dot{\gamma}_1). \end{cases} \tag{8}$$

The constitutive relation $\sigma_h(\dot{\gamma})$ is thus a multivalued function with two separated branches (Fig. 15). This model has five parameters: the viscosity η_1 of the nascent fluid, the viscosity η_2 and "yield stress" A of the shear-induced structure, the shear rate $\dot{\gamma}_1$ above which the shear-induced structure can appear and κ the non local coefficient in [8,18,38].

The homogenous term $\sigma_h(\dot{\gamma})$ is the constitutive curve for an ideal pure shear flow. To it we have added a contribution to the stress due to changes in the shear rate over length scales of the order of the range of interactions between the mesoscopic entities in the system. Since microstructural order is then significantly different in adjacent sliding layers of fluid one expects a correspondingly different response; to lowest order this shows up as a second order derivative. This "diffusive" term $\kappa \partial^2 \dot{\gamma} / \partial^2 z$ smooths the properties at the interface between the bands.

One can also derive such a term by considering an explicit equation of motion for a microstructural shear stress variable σ_m, as follows:

$$\sigma = \sigma_m + \eta \dot{\gamma}, \tag{9}$$

$$\partial_t \sigma = -\frac{1}{\tau}[\sigma_m - \tilde{\sigma}_h(\dot{\gamma})] + \mathcal{D}\frac{\partial^2 \sigma_p}{\partial^2 z}, \tag{10}$$

where σ is the total shear stress, η is a Newtonian viscosity, and $\tilde{\sigma}_h(\dot{\gamma})$ is nonlinear function that expresses the dependence of the microstructural stress σ_m on shear rate. In steady state, the shear stress obeys $\sigma=A$ in simple shear flow or $\sigma=Gz$ in pressure driven flow. In either case, one can eliminate the microstructure stress from the total stress, to obtain Eq. (7) with $\sigma_h=\tilde{\sigma}_h+\eta\dot{\gamma}$ and $\kappa=\mathcal{D}\tau$. Note that such a simple correspondence does not hold for more complex flows.

In the following, we focus on two geometries commonly encountered in rheology: simple shear flow between two infinite plates and planar Poiseuille flow. We will analyze various kind of boundary conditions.

In simple shear flow, we will assume a wall shear rate given by that of the homogeneous constitutive curve at the given (selected) stress. In Poiseuille flow, we will assume a given shear rate at the wall. We will use this boundary condition in Sec. VI to compare our data with the model. In this section we will assume a Newtonian behavior near the wall in order to demonstrate the principles. In both geometries (simple shear flow and Poiseuille flow), we will also present the results for zero shear-rate gradient boundary conditions, as is often used in non local models (analogous to the zero gradient in micellar stress typically used in [9]).

A. Simple shear flow

In simple shear flow the shear stress is a constant, σ_0. Using the dimensionless variable $z_e=z/e$ where e is the gap between the two surfaces, this model leads to

$$\sigma(z_e) = \sigma_0 = \sigma_h[\dot{\gamma}(z_e)] - N_l\frac{\partial^2 \dot{\gamma}(z_e)}{\partial^2 z_e}, \tag{11}$$

$$N_l = \frac{\kappa}{e^2}, \tag{12}$$

where $\dot{\gamma}(z_e)=\frac{\partial V(z_e)}{\partial z_e}$. The shear stress is given by inverting $\dot{\gamma}_h(\sigma)=\dot{\gamma}_h(\sigma)=\sigma_h^{-1}(\dot{\gamma})$, and is multivalued for a range of shear stress. Shear banding is possible in multivalued range, as an inhomogeneous differentiable solution to Eq. (11) with the nascent fluid is at $z_e=0$ and the shear-induced structure at $z_e=1$. Equation (11) requires boundary conditions. We assume no slip at the wall, and a wall shear rate given by that of the homogeneous constitutive curve at the given (selected) stress. That is, we set $\dot{\gamma}_{\text{wall}}=\dot{\gamma}_h(\sigma_0)$, where σ_0 is the (homogeneous) selected shear stress at the wall, and choose the two walls to lie on different branches of the multivalued function. Note that, in the multivalued range, homogeneous solutions may be found by assuming that the fluid follows the pure shear flow rheological curve near the walls, and that both walls are in contact with the nascent fluid or with the shear-induced structure.

The solution is presented in the Appendix. From the calculation of the velocity profile, we can extract the global flow curve of applied shear stress as a function of average shear rate (velocity of the upper plate divided by the size of the gap) as would be measured by a rheometer. Figure 16 shows the flow curves for various values of the nonlocal parameter N_l. Homogeneous flows (thinnest line corresponding to the σ_h function) are obtained at low and high shear stress, whereas heterogeneous flow (thick lines) are obtained for intermediate values. The curves depend significantly on N_1, and hence the size of the gap; a value of $N_l=2\times10^{-2}$ is sufficient to induce deviations from the flow curve. In the limit $N_1\to0$ local parameter N_l, this model selects a single value of the shear stress for the heterogeneous state equal to (see Appendix):

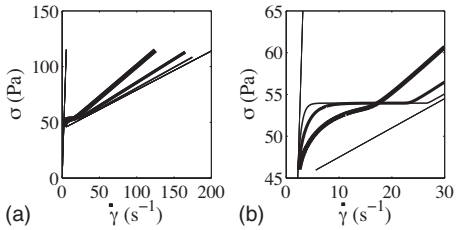

FIG. 16. Global flow curves in steady shear flow for various value of N_l calculated following the procedure detailed in the text. We set $\dot{\gamma}_{\text{wall}}=\dot{\gamma}_h(\sigma_0)$, where σ_0 is the (homogeneous) selected shear stress at the wall, and choose the two walls to lie on different branches of the multivalued function. The two thinnest lines correspond to the σ_h function. They describe homogeneous states, which do not depend upon N_l. The solid lines correspond to the heterogeneous states for (from thickest to the thinnest) $N_l=0.1,10^{-2},10^{-3}$ Right: zoom of the Plateau region.

$$\sigma^* = \dot{\gamma}\sqrt{\eta_1\eta_2} + \frac{A}{1+\sqrt{\eta_2/\eta_1}}. \tag{13}$$

For small values of N_l the flow curve is continuous, while for larger values the flow curve is not continuous; this qualitative feature was also found in [9] in a study of the dJS model, and a recent shear banding calculation by Cook *et al.*, who calculated a smooth variation for a relatively large nonlocal coefficient [39].

The discontinuity in the flow curve comes from the difference between a homogeneous flow of the shear-induced structure and a heterogeneous (shear banding) flow where the shear-induced structure coexists with a thin layer of the nascent structure. This behavior is due to the influence of the boundary condition [9,20]. In the first case the shear rate at the wall is large and given by $(\dot{\gamma}_1\eta_1-A)/\eta_2$ whereas in the second case it is low and given by $\dot{\gamma}_1$. For large N_l the boundary condition affects a larger fraction of the gap, $z/e \simeq \sqrt{N_1}$. This explains the differences of velocity at the wall between the homogeneous flow of the shear-induced structure, and the heterogeneous flow with a very thin layer of the nascent fluid and the discontinuity of the flow curve for large values of the nonlocal parameter. A similar argument applies for an homogeneous flow of the nascent fluid and an heterogeneous flow with a thin layer of the shear-induced structure.

We have also considered a homogeneous boundary condition, $\partial\dot{\gamma}/\partial z=0$ near the walls [8]. In the limit $N_l\to0$ the same selected stress results.

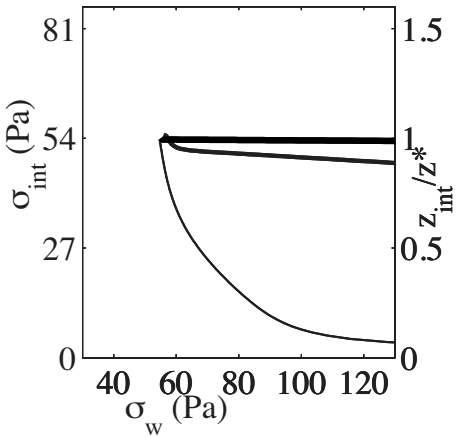

FIG. 17. Shear stress at the interface between the two bands and z_{int}/z^* as a function of the shear stress at the wall in a Poiseuille flow. From thicker to thinner lines, N_l is given by $N_l = 10^{-5}, 10^{-3}, 10^{-1}$. Near the wall, the fluid is assumed to be Newtonian with prescribed wall stress and viscosity $\eta_3 = 1$ Pa s. The other parameters are $\eta_1 = 20.6$ Pa s, $\eta_2 = 0.35$ Pa s, $A = 44$ Pa, $\gamma_1 = 5.6$ s^{-1}.

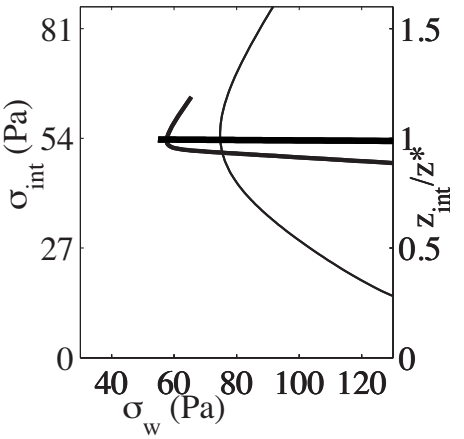

FIG. 18. Shear stress at the interface between the two bands and z_{int}/z^* as a function of the shear stress at the wall. The dashed lines correspond to the wall shear stress whereas the solid lines correspond to the stress at the interface. From thicker to thinner lines, N_l is given by $N_l = 10^{-5}, 10^{-3}, 10^{-1}$. Near the wall, we assume a zero gradient boundary condition. The other parameters are given by $\eta_1 = 20.6$ Pa s, $\eta_2 = 0.35$ Pa s, $A = 44$ Pa, $\gamma_1 = 5.6$ s^{-1}.

B. Poiseuille flow

Let us now focus on the planar Poiseuille geometry, where a pressure drop ΔP or equivalently a wall shear stress σ_w drives flow between two surfaces separated by a gap $2e$ in the z direction. In this geometry, the shear stress is a linear function of the distance from the center of the gap. Using the dimensionless variable $z_e = z/e$, the condition of a linear stress imposes the following differential equation on the shear rate:

$$\sigma(z_e) = \sigma_w z_e = \sigma_h[\dot{\gamma}(z_e)] - N_l \frac{\partial^2 \dot{\gamma}(z_e)}{\partial^2 z e}, \tag{14}$$

where, in the thin and long (length L) gap limit, $\sigma_w = \Delta P e/L$ is the wall stress. The shear rate satisfies $\partial\dot{\gamma}/\partial z|_{z_e=0} = 0$ (at the center of the gap) by symmetry. In order to discuss the model, at the wall we will arbitrarily either assume that the high shear-rate phase lies near the wall with a Newtonian viscosity η_3 or zero gradient. The analytic solutions are given in the Appendix.

Figure 17 presents the value of the shear stress at the interface and the shear stress at the wall as a function of the position of the interface for various values of N_l. Near the wall, the fluid is assumed to be Newtonian with prescribed wall stress and viscosity $\eta_3 = 1$ Pa s. The other parameters are given by $\eta_1 = 20.6$ Pa s, $\eta_2 = 0.35$ Pa s, $A = 44$ Pa, $\gamma_1 = 5.6$ s^{-1}.

For smaller $N_l = 10^{-5}$, the shear stress at the interface is independent of the wall stress, and equal to σ^* (Fig. 17), as was suggested in [21]. For larger N_l the shear stress at the interface varies with applied wall stress), and decreases when the size of the shear-induced structure increases. Values as low as $N_l = 10^{-3}$ can induce a large effect. This result suggests that the asymptotic analysis of Radulescu *et al.* [21] is limited to a smaller range of N_l than suggested in that work. Figure 17 highlights a very important point: for the same shear stress at the wall, the shear-induced phase will fill a large part of a small capillary tube (very large N_l) and a very small part of a large one (much smaller N_l).

Finally, we have performed the same analysis assuming a zero gradient boundary condition. Figure 18 shows similar results to the previously chosen BC. The shear stress at the interface varies with applied shear stress. We note however that for large N_l, the value of the shear stress at the wall decreases when the size of the high sheared band increases and the interface thus moves away from the wall.

VI. COMPARISON BETWEEN THE MODEL AND THE DATA AND DISCUSSIONS

Figures 5, 9, and 11 compare the velocity profiles from our model with the experimental data. To fit the data, boundary conditions (i.e., velocity slip at the wall and shear rate at the wall) were required. This question is a key point. At this stage and to the best of our knowledge, there is no consensus about the correct boundary condition to handle the non local (diffusive) term. In the scalar model we use this is a boundary condition on the shear rate (in addition to the required boundary condition for the velocity). Typical choices could be a zero gradient in shear rate (analogous to the zero gradient in micellar stress typically used, e.g., in [9]). Another possibility is an imposed "surface viscosity," so that the surface follows, for example the constitutive behavior of one or the other shear branches, or something else characteristic of the surface. Here, we take a more empirical approach, and use the boundary conditions that are measured. One reason for this is that the strong shear stress gradient near the walls, in Poiseuille flow, is quite strong. Hence we measure the values of the shear rate at the wall, as determined by a linear fit of the last three points of the velocity profiles near the walls (see Figs. 14 and 13). Clearly, these measurements do not correspond to the bulk rheology and depend upon the

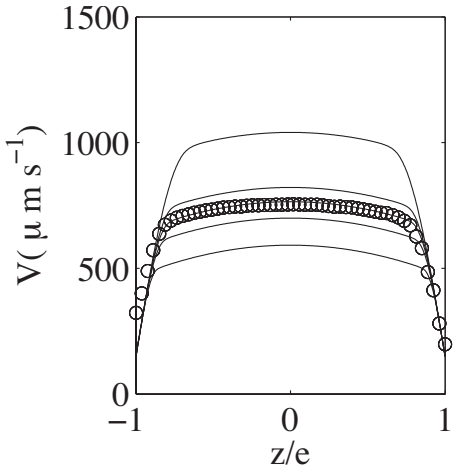

FIG. 19. Velocity profile for $\sigma_w=73$, channel width $2e=200$ μm with rough surface R2. Solid lines are calculated using the nonlocal model described in Sec. V. From top to bottom $\kappa=310^{-10}$, 1.2510^{-10}, 10^{-10}, 7.510^{-10}, 3.310^{-11}. The other parameters are given by $\eta_1=20.6$ Pa s, $\eta_2=0.35$ Pa s, $A=44$ Pa, $\gamma_1=5.6$ s^{-1}.

nature of the surface. We use these experimental data as boundary conditions together with the measured slip velocity boundary condition. A single set of parameters ($\eta_1=20.6$ Pa s, $\eta_2=0.35$ Pa s, $A=44$ Pa, $\gamma_1=5.6$ s^{-1}, $\kappa=10^{-10}$ Pa s m^2) allows us to fit all the profiles. For this value of κ the nonlocal parameter N_l lies between 10^{-2} and 2×10^{-3} for different channel widths.

To give an idea of the precision of the fit, Fig. 19 shows for a typical velocity profile the role of the parameter κ. Keeping all the others parameter constant we have varied this parameter by a factor of 3, 1.25, 0.75, and 1/3. Clearly, the velocity profiles depend strongly upon this parameter. Our procedure allows us to measure it with a better precision than 25%.

Moreover to measure the quality of our fitting procedure, we have computed the standard deviation of the difference between the experimental velocity profile and the theoretical one. We recall that standard deviation of vector V is equal to std $V=\sqrt{(\frac{1}{N-1}\Sigma_{i=1}^{n}(V_i-\bar{V})}$, where $\bar{V}$ is the mean value of V and N the number of data points. For each profile, we find a standard deviation of less than 4% of the maximal velocity.

In addition, with this set of parameters we can fit the bulk flow curve by approximating the cone-and-plate geometry, which has a nearly uniform stress, by the uniform shear stress of planar shear flow (see Appendix). From the value of the shear curvature viscosity, one can estimate a characteristic length $\xi=\sqrt{(\kappa/\eta(\dot{\gamma}))}$. In the plateau region ξ varies from 1 to 10 μm in agreement with recent indirect measurements on the same system [25]. At first sight, this length is much larger (50 times) than the one measured by Radulescu *et al.* using kinetic experiments on CTAB-NaNO3 [40]. However these discrepancies seem related to the difficulty of properly separating the kinetic steps involved in the displacement of the interface (instability, reconstruction, and front propagation). It seems that a more complete analysis leads to μm size length scale for this system also [41].

This length is much larger than the typical mesh size $\xi_{mesh}=(\frac{kbT}{G})^{1/3}$ of these solutions which can be estimated by using the elastic modulus G of the solution. For our system, $G=70$ Pa and $\xi_{mesh}=39$ nm.

A candidate physical mechanism for the nonlocal term is local concentration fluctuations in the highly sheared band. In visible light microscopy the high shear band appears to be black [10] in transmission, suggesting significant scattering due, for example, to concentration fluctuations on μm scales or larger. These concentration fluctuations are observed even without particles. This suggests that the correlation length exists even without particles and is not correlated with the size of the particles. ξ is much smaller than the gap (0.5–1 mm) or curvature radii (cm) of classical rheometers, so that nonlocal effects cannot be detected in these geometries, even by performing local measurements. Note also that ξ is closed to the depth of the rough surfaces. This may explain the strong effect of the ruguous walls on the surface rheology.

VII. CONCLUSION

Our work shows that nonlocal model is required to capture the behavior of wormlike micellar system in a small gap. We have used a phenomenological model. More work need to be done to describe the high sheared branch. The two species model introduced recently by Cook and co-workers may be good candidates as it predicts a Bingham behavior for the high sheared branch.

Our work highlights the fundamental role of the surfaces on the flow of wormlike micellar solutions. This point is not limited to the semidilute wormlike micellar solution of this study. Recently, it has been shown that surfaces govern the flow behavior in laponite solution [44], concentrated emulsions [45,46], and concentrated wormlike micellar solutions [47]. In all cases, the slip velocity is affected by the roughness of the surface. More strikingly, the wall shear rate for a given wall shear stress varies as a function of the nature of the surface. This suggests the existence of a surface rheological law; i.e., a nontrivial relationship between the wall shear stress and the wall shear rate, which differs from the bulk rheological law and depends upon the nature of the surface. Experiments to better measure the flow and flowing microstructure very close to solid surfaces will thus open avenues for modeling the rheological behavior of wormlike micelles near a surface, and help determine the proper boundary conditions for the fluids.

ACKNOWLEDGMENTS

We thank J. B Salmon for useful discussions and help in performing the PIV experiments. We acknowledge funding from Rhodia and from the Région Aquitaine and GIS Matériaux.

APPENDIX

In this appendix we present the details of the calculations in both simple shear and Poiseuille flows. For simple shear, we will assume that shear rate is fixed to low or high shear

branch. For Poiseuille flow, we will calculate the flow assuming zero shear gradient or imposed wall shear rate near the wall.

1. Simple shear flow

We first focus on simple shear flow between infinite plates, for which the shear stress is constant, σ_0. Using the dimensionless variable $z_e=z/e$ where e is the gap between the two surfaces, this model leads to

$$\sigma(z_e)=\sigma_0=\sigma_h[\dot{\gamma}(z_e)]-N_l\frac{\partial^2\dot{\gamma}(z_e)}{\partial^2 z_e}, \tag{A1}$$

$$\dot{\gamma}(z_e)=\frac{\partial V(z_e)}{\partial z_e}. \tag{A2}$$

where $N_l=\frac{\kappa}{e^2}$ is the dimensionless nonlocal parameter. To compute the shear-rate field $\dot{\gamma}(z_e)$ we require boundary conditions for the shear rate. The velocity field is assumed to obey a no-slip condition, but the nonlocal term demands an additional condition on the shear rate. Many different choices are possible, depending on the nature of the surface interaction. In principle the correct boundary condition should follow from mechanical balance at the wall [20]. Possibilities include a zero gradient $\partial\dot{\gamma}/\partial z_e=0$; a fixed value $\dot{\gamma}(0)$; or a more complex expression. Here, we will assume a simple form to illustrate the importance of the nonlocal term.

Hence, we assume that near the surfaces, the fluid follows the rheological curve set by $\sigma=\sigma_h(\dot{\gamma})$.

(a) For $\sigma_0<\eta_2\dot{\gamma}_1+A$, we demand $\dot{\gamma}(z_e)=\sigma_0/\eta_1$ for $z_e=0,1$. In this case a homogeneous solution results, corresponding to the nascent structure, $\dot{\gamma}(z_e)=\sigma_0/\eta_1$.

(b) For $\sigma_0>\eta_1\dot{\gamma}_1$, we demand $\dot{\gamma}(z_e)=(\sigma_0-A)/\eta_2$ for $z_e=0,1$. In this case, we obtain a homogeneous solution corresponding to the shear-induced structure, $\dot{\gamma}(z_e)=(\sigma_0-A)/\eta_2$.

(c) For $\eta_2\dot{\gamma}_1+A>\sigma_0>\eta_1\dot{\gamma}_1$, the constitutive curve is multivalued (Fig. 15) so that for a range of shear stresses two different shear rates may be found at the walls: either the low (nascent) or high (shear-induced) shear-rate branches of the fluid. Banded flows obtain if one wall prescribes the nascent fluid and the other wall prescribes the shear-induced fluid,

$$\dot{\gamma}(0)=\sigma_0/\eta_1, \tag{A3}$$

$$\dot{\gamma}(1)=(\sigma_0-A)/\eta_2 \tag{A4}$$

(or vice versa).

The solution for a continuous shear-rate field with a single interface can be written as

$$\dot{\gamma}(z_e)=\begin{cases}\dfrac{\sigma_0}{\eta_1}+\left(\dot{\gamma}_1-\dfrac{\sigma_0}{\eta_1}\right)\dfrac{\sinh(X_1 z_e)}{\sinh(X_1 a)} & (z_e<a)\\ \dfrac{\sigma_0-A}{\eta_2}+\left(\dot{\gamma}_1-\dfrac{\sigma_0-A}{\eta_2}\right)\dfrac{\sinh[X_2(z_e-1)]}{\sinh[X_2(a-1)]} & (z_e>a),\end{cases} \tag{A5}$$

where $X_i=\sqrt{\frac{\eta_i}{N_l}}$ and a is the position of the interface between the nascent structure and the shear-induced structure. Demanding continuity of the derivative of the shear rate $\dot{\gamma}(z_e)$ at the interface $z_e=a$ leads to a condition that determines the selected shear stress $\sigma^*\equiv\sigma_0$ at which shear banding occurs,

$$\left(\dot{\gamma}_1-\frac{\sigma^*}{\eta_1}\right)\frac{X_1\tanh[X_2(a-1)]}{X_2\tanh(X_1 a)}=\left(\dot{\gamma}_1-\frac{\sigma^*-A}{\eta_2}\right). \tag{A6}$$

For finite systems the shear stress changes as the interface between shear bands approaches the wall, while in an infinite system the shear stress is unchanged. In the limit $N_l\to 0$, this condition can be written as

$$\sigma^*=\dot{\gamma}_1\sqrt{\eta_1\eta_2}+\frac{A}{1+\sqrt{\eta_2/\eta_1}}+\epsilon\frac{\sqrt{\eta_1\eta_2}}{(\sqrt{\eta_1}+\sqrt{\eta_2})^2}[\dot{\gamma}(\eta_1-\eta_2)+A]+\cdots, \tag{A7}$$

$$\epsilon=2[e^{-X_2(1-a)}-e^{-X_1 a}]. \tag{A8}$$

These equations then determine the velocity field, assuming no slip at the wall $V(0)=0$,

$$V(z_e)=\begin{cases}\dfrac{\sigma^* z_e}{\eta_1}+\left(\dot{\gamma}_1-\dfrac{\sigma^*}{\eta_1}\right)\dfrac{\cosh(X_1 z_e)-1}{X_1\sinh(X_1 a)} & (z_e<a)\\ \dfrac{(\sigma^*-A)z_e}{\eta_2}+\left(\dot{\gamma}_1-\dfrac{\sigma^*-A}{\eta_2}\right)\dfrac{\cosh[X_2(z_e-1)]}{X_2\sinh[X_2(a-1)]}+V_V & (z_e>a),\end{cases} \tag{A9}$$

$$V_V = \left(\dot{\gamma} - \frac{\sigma^*}{\eta_1}\right)\left[\frac{(1-\eta_1/\eta_2)\cosh X_1 a - 1}{(1+\sqrt{\eta_1/\eta_2})X_1 \sinh X_1 a}\right] + \left[\sigma^*\left(\frac{1}{\eta_1} - \frac{1}{\eta_2}\right) + \frac{A}{\eta_2}\right]a. \tag{A10}$$

From this we can calculate the velocity V_w at the moving wall,

$$V_w = \frac{(\sigma^* - A)}{\eta_2} + \left(\dot{\gamma}_1 - \frac{\sigma^* - A}{\eta_2}\right)\frac{1}{X_2 \sinh(X_2(a-1)} + V_V. \tag{A11}$$

and thus the global flow curve.

2. Poiseuille flow

Here we consider pressure-driven Poiseuille flow between flat parallel plates, in which the shear stress is a linear function of the distance z from the midpoint between the plates (we assume a symmetric velocity profile). Using the dimensionless variable $z_e = z/e$ where $2e$ is the gap between the two surfaces, the strain rate must thus satisfy the following differential equation:

$$\sigma(z_e) = \sigma_w z_e = \sigma_h[\dot{\gamma}(z_e)] - N_l \frac{\partial^2 \dot{\gamma}}{\partial z_e^2}, \tag{A12}$$

where the wall stress, in the limit of an infinitely long channel with wide aspect ratio, is given by $\sigma_w = \Delta P e/L$. We will cast the rest of the results in terms of this idealized wall stress; conversion to pressure difference or pressure gradient is straightforward. By symmetry we must have

$$\dot{\gamma}(z_e = 0) = 0. \tag{A13}$$

As previously, the choice of boundary condition as the wall will drive the flow. We present two calculations: zero gradient at the wall, and a specified wall shear rate $\dot{\gamma}_w$.

a. Imposed wall shear rate $\dot{\gamma}_w$

If we assert that the wall specifies a certain shear rate, then the boundary condition is

$$\dot{\gamma}(z_e = 1) = \gamma_w. \tag{A14}$$

The shear-rate field that satisfies the boundary conditions, and switches between flow branches such that $\dot{\gamma}(z_e = a) = \dot{\gamma}_1$ is

$$\dot{\gamma}(z_e) = \begin{cases} \dfrac{\sigma_w z_e}{\eta_1} + \left(\dot{\gamma}_1 - \dfrac{\sigma_w a}{\eta_1}\right)\dfrac{\sinh(X_1 z_e)}{\sinh(X_1 a)} & (z_e < a) \\ \dfrac{\sigma_w z_e - A}{\eta_2} + \left(\dot{\gamma}_1 - \dfrac{\sigma_w a - A}{\eta_2}\right)\dfrac{\sinh[X_2(z_e-1)]}{\sinh[X_2(a-1)]} + \left(\dot{\gamma}_w - \dfrac{\sigma_w - A}{\eta_2}\right)\dfrac{\sinh X_2(a-z_e)}{\sinh X_2(a-1)} & (z_e > a), \end{cases} \tag{A15}$$

where a is the position of the interface between the nascent and shear-induced phases. Continuity of the derivative $\dot{\gamma}'(z_e)$ at the interface $z_e = a$ relates the interface position a to the wall stress σ_w (the analog of stress selection),

$$\sigma_w\left(\frac{1}{\eta_1} - \frac{1}{\eta_2}\right) + \left(\dot{\gamma}_1 - \frac{\sigma_w a}{\eta_1}\right)X_1 \coth X_1 a = \left(\dot{\gamma}_w - \frac{(\sigma_w - A)}{\eta_2}\right)\frac{X_2}{\sinh X_2(1-a)} - \left(\dot{\gamma}_1 - \frac{(\sigma_w a - A)}{\eta_2}\right)X_2 \coth X_2(1-a). \tag{A16}$$

Figure 17 shows an example of the relation between the stress at the interface, $\sigma_{int} = \sigma_w a$, and the wall stress σ_w (assuming that the rheology at the wall follows Newtonian behavior).

In wide geometries, i.e., for vanishing values of the non local parameter N_l, this condition leads the same selected stress as in simple shear flow, such that the shear stress at the interface satisfies $\sigma_w a = \sigma^*$, with σ^* given by Eq. (A8).

$$\sigma^* = \left[\dot{\gamma}\sqrt{\eta_1 \eta_2} + \frac{A}{1+\sqrt{\eta_2/\eta_1}}\right]\left[1 - \frac{1}{a}\sqrt{\frac{D}{\eta_2}}\frac{1}{1+\sqrt{\eta_2/\eta_1}} + \cdots\right], \tag{A17}$$

where the expansion is in the small N_l limit, such that the interface is sufficiently far from either the walls or the center of the cell, $X_1 a \ll 1, X_2(1-a) \ll 1$.

The velocity profile follows by integrating the shear-rate field, Eq. (A14) with boundary condition $V(z = \pm 1) = 0$,

$$V(z_e) = \begin{cases} \dfrac{\sigma_w z_e^2}{2\eta_1} + \left(\dot{\gamma}_1 - \dfrac{\sigma_w a}{\eta_1}\right)\dfrac{\cosh(X_1 z_e)}{X_1 \sinh(X_1 a)} + V & (z_e < a) \\ \dfrac{\sigma_w z_e^2 - 2A z_e}{2\eta_2} + \left(\dot{\gamma}_1 - \dfrac{\sigma_w - A}{\eta_2}\right)\dfrac{\cosh[X_2(z_e-1)]}{X_2 \sinh[X_2(a-1)]} - \left(\dot{\gamma}_w - \dfrac{\sigma_w - A}{\eta_2}\right)\dfrac{\cosh X_2(a-z)}{X_2 \sinh X_2(a-1)} & (z_e > a), \end{cases} \tag{A18}$$

$$V = V_2(a) - \frac{\sigma_w a^2}{2\eta_1} - \left(\dot{\gamma}_1 - \frac{\sigma_w a}{\eta_1}\right)\frac{\cosh(X_1 a)}{X_1 \sinh(X_1 a)}. \tag{A19}$$

We have used formula (A19) to fit our measurements.

b. Zero gradient $\gamma' = 0$

Another choice of boundary condition is zero gradient, boundary condition is

$$\dot{\gamma}'(z_e = 1) = 0. \tag{A20}$$

In this case the solutions are

$$\dot{\gamma}(z_e) = \begin{cases} \dfrac{\sigma_w z_e}{\eta_1} + \left(\dot{\gamma}_1 - \dfrac{\sigma_w a}{\eta_1}\right)\dfrac{\sinh(X_1 z_e)}{\sinh(X_1 a)} & (z_e < a) \\ \dfrac{\sigma_w z_e - A}{\eta_2} + \left(\dot{\gamma}_1 - \dfrac{\sigma_w a - A}{\eta_2}\right)\dfrac{\cosh X_2(1 - z_e)}{\cosh X_2(1 - a)} - \dfrac{\sigma_w}{X_2 \eta_2}\dfrac{\sinh X_2(z_e - a)}{\sinh X_2(1 - a)} & (z_e > a), \end{cases} \tag{A21}$$

and the stress selection condition, determined by continuity of the derivative $\dot{\gamma}'$, is

$$\sigma_w = \frac{\eta_2 \dot{\gamma}_1 [1 + \sqrt{\eta_1/\eta_2}\coth X_1 a \coth X_2(1 - a)] + A}{\dfrac{(1 - \eta_2/\eta_1)\coth X_2(1 - a) - \operatorname{csch} X_2(1 - a)}{X_2} + a[1 + \sqrt{\eta_2/\eta_1}\coth X_1 a \coth X_2(1 - a)]}. \tag{A22}$$

[1] R. G. Larson, *The Structure and Rheology of Complex Fluids* (Oxford University Press, New York, 1999).
[2] M. E. Cates *et al.*, Macromolecules **20**, 2289 (1987).
[3] M. E. Wunderlich, H. Hoffmann, and H. Rehage, Rheol. Acta **26**, 532 (1987).
[4] M. M. Britton and P. T. Callaghan, Phys. Rev. Lett. **78**, 4930 (1997).
[5] S. Lerouge, J. P. Decruppe, and C. Humbert, Phys. Rev. Lett. **81**, 5457 (1998).
[6] J. B. Salmon, A. Colin, S. Manneville, and F. Molino, Phys. Rev. Lett. **90**, 228303 (2003).
[7] C.-Y. D. Lu, P. D. Olmsted, and R. C. Ball, Phys. Rev. Lett. **84**, 642 (2000).
[8] P. D. Olmsted and C.-Y. D. Lu, Faraday Discuss. **112**, 183 (1999).
[9] P. Olmsted, O. Radulescu, and C.-Y. D. Lu, J. Rheol. **44**, 257 (2000).
[10] C. Masselon, J. B. Salmon, and A. Colin, Phys. Rev. Lett. **100**, 038301 (2008).
[11] N. A. Spenley, M. E. Cates, and T. C. B. McLeish, Phys. Rev. Lett. **71**, 939 (1993).
[12] G. Porte, J. F. Berret, and J. L. Harden, J. Phys. II **7**, 459 (1997).
[13] T. C. B. McLeish, J. Polym. Sci., Part B: Polym. Phys. **25**, 2253 (1987).
[14] J. Krug, J. L. Lebowitz, H. Spohn, and M. Q. Zhang, J. Stat. Phys. **44**, 535 (1986).
[15] J. R. A. Pearson, J. Rheol. **38**, 309 (1994).
[16] P. D. Olmsted and P. M. Goldbart, Phys. Rev. A **41**, 4578 (1990).
[17] P. D. Olmsted and C.-Y. D. Lu, Phys. Rev. E **56**, R55 (1997).
[18] J. K. G. Dhont, Phys. Rev. E **60**, 4534 (1999).
[19] A. W. El-Kareh and L. G. Leal, J. Non-Newtonian Fluid Mech. **33**, 257 (1989).
[20] J. M. Adams, S. M. Fielding, and P. D. Olmsted, J. Non-Newtonian Fluid Mech. **151**, 101 (2008).
[21] O. Radulescu and P. D. Olmsted, Rheol. Acta **38**, 606 (1999).
[22] O. Radulescu, and P. D. Olmsted, J. Non-Newtonian Fluid Mech. **91**, 143 (2000).
[23] L. P. Cook, and L. R. Rossi, J. Non-Newtonian Fluid Mech. **116**, 347 (2004).
[24] L. F. Rossi, G. McKinley, and L. P. Cook, J. Non-Newtonian Fluid Mech. **136**, 79 (2006).
[25] P. Ballesta, M. P. Lettinga, and S. Manneville, J. Rheol. **51**, 1047 (2007).
[26] J. M. White, *Viscous Fluid Flow*, 2nd ed. (McGraw-Hill, New York, 1991).
[27] P. Guillot, P. Panizza, J. B. Salmon, M. Joanicot, A. Colin, C. H. Bruneau, and T. Colin, Langmuir **22**, 6438 (2006).
[28] D. C. Duffy, J. C. McDonald, O. J. A. Schueller, and G. M. Whitesides, Anal. Chem. **70**, 4974 (1998).
[29] J. G. Santiago, S. T. Wereley, C. D. Meinhart, D. J. Beebe, and R. J. Adrian, Exp. Fluids **25**, 316 (1998).
[30] M. Collins, and W. R. Schowalter, AIChE J. **9**, 98 (1963).
[31] G. Degré, P. Joseph, P. Tabeling, S. Lerouge, M. Cloitre, and A. Ajdari, Appl. Phys. Lett. **89**, 024104 (2006).
[32] J. F. Berret, G. Porte, and J. P. Decruppe, Phys. Rev. E **55**, 1668 (1997).
[33] R. W. Mair and P. T. Callaghan, J. Rheol. **41**, 901 (1997).
[34] A. F. Mendez-Sanchez, J. Perez-Gonzales, L. de Vargas, J. R. Castrejon-Pita, A. A. Castrejon-Pita, and G. Huelsz, J. Rheol. **47**, 1455 (2003).
[35] M. M. Britton and P. T. Callaghan, Eur. Phys. J. B **7**, 237 (1999).

[36] M. Johnson and D. Segalman, J. Non-Newtonian Fluid Mech. **2**, 255 (1977).
[37] D. S. Malkus, J. S. Nohel, and B. J. Plohr, J. Comput. Phys. **87**, 464 (1990).
[38] N. A. Spenley, X. F. Yuan, and M. E. Cates, J. Phys. II **6**, 551 (1996).
[39] L. Zhou, P. A. Vasquez, L. P. Cook, and G. A. McKinley, J. Rheol. **52**, 591 (2008).
[40] O. Radulescu, P. D. Olmsted, J. P. Decruppe, S. Lerouge, J. F. Berret, and G. Porte, Eur. Phys. Lett **62**, 230 (2003).
[41] S. Lerouge (private communication).
[42] P. Nghe, G. Degré, P. Tabeling, and A. Ajdari, Appl. Phys. Lett **93**, 204102 (2008).
[43] M. E. Helgeson, P. A. Vasquez, E. W. Kaler, and N. J. Wagner, J. Rheol. **53**, 727 (2009).
[44] T. Gibaud, C. Barentin, and S. Manneville, Phys. Rev. Lett. **101**, 258302 (2008).
[45] J. Goyon, A. Colin, G. Ovarlez, A. Ajdari, and L. Bocquet, Nature **454**, 84 (2008).
[46] S. P. Meeker, R. T. Bonnecaze, and M. Cloitre, Phys. Rev. Lett. **92**, 198302 (2004).
[47] L. Bécu, S. Manneville, and A. Colin, Phys. Rev. Lett. **93**, 018301 (2004).